Inherited state of stress as a key factor controlling slip and slip mode: inference from the study of a slow slip event in the Longitudinal Valley, Taiwan

Alexandre Canitano[1], Maxime Godano[2] and Marion Y. Thomas[3]

Contents of this file

1. Text S1 to S3

Corresponding author: A. Canitano, Institute of Earth Sciences, Academia Sinica, P.O Box 1-55, Nankang, Taipei, Taiwan. (canitano@earth.sinica.edu.tw)

[1]Institute of Earth Sciences, Academia Sinica, Nankang, Taipei, Taiwan.

[2]Université Côte d'Azur, CNRS, Observatoire de la Côte d'Azur, IRD, Géoazur, 250 rue Albert Einstein, Sophia Antipolis 06560 Valbonne, France.

[3]Sorbonne Université, CNRS-INSU, Institut des Sciences de la Terre Paris, ISTeP UMR 7193, F-75005 Paris, France.

2. Tables S1 to S2

3. Figure S1 to S15

Introduction

We include here 2 tables, 15 figures and 3 sections: (S1) details the grid-search approach for SSE source characterization, (S2) describes the geodetic template matching for detection of recurrent SSEs, and (S3) details the multiplet source radius estimates and uncertainties.

S1: Grid-search approach for SSE source characterization

We search for a source compatible with the LVF (strike=23°, rake=70°) and adopt the listric fault geometry defined by *Thomas et al.* [2014] that is a dip angle decreasing gradually from 60° at 0-14 km to 45° at 14-22 km and to 30° at 22-27 km. Since the strain amplitudes recorded by ZANB and SSTB are within the same order of magnitude, the source is likely located in the region between these two stations. We explore the area of 40 km NS over 22 km EW (from reference station FBRB) which covers the region between the two networks and accounts for the deeper extent of the LVF. The selection process of the best source model is performed following the aforementioned steps:

1 : The search is performed over the entire grid (40 km x 22 km x 27 km) for the parameters detailed in Table S1 with horizontal and vertical spacings of 0.5 km and 1 km, respectively. At each step, we calculate the dilatation at the sensor locations (for the mean depth of 200 m) resulting from a static dislocation in an elastic homogeneous

half-space for a planar rectangular fault with uniform slip [*Okada*, 1992]. A total of 6.10^8 source models are calculated with geodetic moment magnitude ranging from 3.30 to 7.15.

2 : The optimal source model is searched on the grid nodes following a protocol derived from GPS source modeling [*Lin et al.*, 2019]. For a given source centered at the node i, the misfit (in nϵ) is calculated by root mean square (rms) error:

$$misfit_i = \sqrt{\frac{\sum_{k=1}^{n}(d_k^i - D_k)^2}{n}} \qquad (1)$$

where d_k^i represents the modeled dilatation for the k^{th} strainmeter location for a source centered at the node i, D_k is the observed dilatation for the k^{th} strainmeter, and n denotes the number of observations ($n = 4$, 1 observation per station).

3 : To improve the source location and magnitude, a second grid search is performed starting from locations and sources parameters associated with the lowest misfit values by reducing the grid horizontal and vertical nodes spacings (0.25 km), source dimensions (0.5 km) and aseismic slip (1 cm).

4 : Horizontal and vertical surface displacements associated with the selected optimal models are computed and compared with observed surface displacements.

After running steps 1 and 2, we found 2 source regions associated with low rms misfit ($<$ 2.2 nϵ): a shallow source ($\sim$ 2-3 km) and a source located at intermediate depth (10-12 km) (Figure S5). Both regions are located on the section of the LVF dipping 60° SE. Next, to improve the source strength and location, we perform a second grid search starting from the location of our preliminary best models (step 3). Our best model for the shallow source (rms misfit = 2.137 nϵ) is located at 1.75 km depth ($E = 3.25$ km, $N = 16.5$

km from FBRB), has dimensions of $L = 15$ km, $W = 3.75$ km ($R = 4$) and $U = 5$ cm (M_w = 5.21). If we allow 5% of uncertainties for the minimum misfit, we find 90 source models within 1.75-2.25 km depth (E = 2.5-3.25 km, N = 16.25-16.75 km from FBRB), with L = 7-15 km, W = 1.7-4.8 km and U = 5-25 cm. We compute the GPS displacements for the source models and find that large east, north and vertical displacements (> 8 mm) are expected at station YUL1 while displacements at other stations remain generally low (< 1 mm). Besides, for the source with the largest dimensions ($L \geq 11$ km), substantial east, north and vertical displacements are also expected for station JULI (> 8 mm) and JPIN (> 4.5 mm). Such amplitudes are larger than the GPS detection threshold and surface displacements should have been detected by the stations (Figure S2). Consequently, a shallow source appears unlikely to be the source of the SSE.

We perform step 3 for the second source, located at intermediate depth. There are numerous sources allowing to explain the strain data well (445 sources show a misfit < 2 nϵ). Considering a rms misfit < 1 nϵ, it remains 16 sources that are located between depths of 10.5 to 11.5 km (E = 6-7.75 km, N = 6-7.5 km from FBRB). Sources have a similar geodetic moment magnitude (M_w = 5.41-5.45) but show large discrepancies in size (L = 16-24 km, W = 3.8-12 km (R = 1.8-4.6)) (Figure S6a). Fault surfaces are ranging from about 65 to 288 km^2 and aseismic slip U is in the range 2-10 cm. Static stress drop estimated from equation (1) shows a difference of about one order of magnitude between small ($\Delta\sigma$ = 0.32 MPa) and large ($\Delta\sigma$ = 0.03 MPa) fault ruptures. We compute the GPS displacements for the 16 source models and find that the maximum displacements are 1.9 and 2 mm for the vertical components at stations PING and CHGO, respectively. Consequently, such sources would remain undetected by GPS and the intermediate-depth section of the LVF represents the likely source region of the SSE. The lowest misfits are achieved (rms < 0.64 nϵ) for sources located at the depth of 10.75 km (E = 6.5-6.75 km, N = 6.25-6.75 km from FBRB). Our preferred source model (rms misfit = 0.36 nϵ) is located at 10.75 km depth, it has length (L) and width (W) of 19 km x 6.4 km, respectively, and a total displacement of $U = 5$ cm ($M_w = 5.44$) (Figure S6a, red circle). Overall, the SSE source location is constrained with a resolution of the order of a kilometer and its depth is particularly well constrained, even with a limited number of stations, as buried sources result in dilatation that changes sign at distances strongly dependent on the source depth. Therefore, insignificant change recorded by FBRB is thus explained by a nodal plane passing through the station location (Figure S6b).

S2: Strainmeter template matching for SSE detection

We implement a template matching for the strainmeter signals (SSTB, ZANB and HGSB). Time-series are downsampled from 1 min to 1 hour. The analysis starts in 02/2004 (HGSB), 08/2004 (ZANB) and 01/2009 (SSTB) and ends in 04/2019 for all stations. The 13-day long SSE signal is selected as template for each station (signal is detided, detrended and corrected for air pressure-induced strain) and we perform sliding window cross-correlations for each station to detect potential repeating slow events. We shift the template window by increments of 2 hrs through the continuous strainmeter time-series, correlate the signals using least squares regression and estimate the correlation coefficient

(R) for each iteration. We can note that SSTB template represents the most robust signal for the detection; it is extensive strain with the largest amplitude (+ 50 nϵ) which can be easily detected as it strongly differs from the crustal strain changes induced by rainfall (i.e., compressive strain). While no data were available for CHMB and SSNB for the 2011 SSE (the stations were not operating), predictions show amplitudes of $\sim$ -12 nϵ and -18 nϵ for CHMB and SSNB, respectively (Figure S6b). These stations would have recorded resolvable signals and can thus be used for visual inspection of potential repeating events.

Figure S7 shows the results for SSTB and ZANB for the period 08/2004-04/2019. We exclude HGSB due to the moderate to low quality of the correlations ($R < 0.75$), likely related to the low amplitude of HGSB signal (about -10 nϵ) which is close to the strain noise level at the period of a few weeks. Further, correction for air pressure-induced strain for the station is limited due to the absence of barometer for HGSB during several years, thus preventing a reliable template matching analysis. In the case of high correlations ($R \geq 0.85$) for SSTB and ZANB, we also inspect signals for other stations but found no recurrent slow signals. Some high correlations are found for ZANB during tropical typhoons such as Saomai (around day 222), Morakot (day 1316), Usagi (day 2821) or Nepartek (day 3842). They can be explained by the fact that volumetric strain signals during rainfall show a contraction (negative sign) which can also coincide with the pattern of ZANB signal during the SSE, despite the latter does not occur during a rainfall episode.

S3: Source radius estimates and uncertainties

The source radius R of each relocated event is estimated based on the relationship between stress drop $\Delta\sigma$ and seismic moment M_0 [*Eshelby*, 1957]:

$$\Delta\sigma = \frac{7}{16}\left(\frac{1}{R}\right)^3 M_0 \tag{2}$$

We convert the event local magnitude M_L to moment magnitude M_w using an empirical formula derived for Taiwan [*Huang et al.*, 2000]:

$$M_w = 0.91 M_L - 0.07 \tag{3}$$

Then, the seismic moment of each earthquake is estimated from the moment magnitude [*Kanamori and Anderson*, 1975]. The mean stress drop is taken as 3.16 MPa with uncertainties of 1-10 MPa based on a previous analysis of $M_L \sim 2.0$ REs in the same fault region [*Canitano et al.*, 2018]. Source radii range between 20 and 90 m (30-40 m for the 3 events in 2011). We assess the influence of stress drop and local magnitude (with maximum error of $\pm$ 0.5 [*Wu et al.*, 2005]) uncertainties on the determination of source radius and infer source radii varying between -40 and +250%.

We then asses the influence of these uncertainties on the source overlapping by following a stochastic approach. For each event:

(i) : we perturb the source location by random values drawn in Gaussian distributions of two standard deviations (2σ) equal to the relative location uncertainty

(ii) : we compute the source radius from (1) stress drop randomly drawn in a log-normal distribution centered on 3.16 MPa with 95% of values within 1-10 MPa and (2) local magnitude changed by a random perturbation drawn in a Gaussian distribution of 2σ equals to 0.5.

The process is repeated 1000 times and the 1000 $\times$ 10 simulated centroids and source radii are projected onto the LVF plane and an average number of ruptures are computed for small cells of 10 $\times$ 10 m.

References

Canitano, A., M. Godano, Y. J. Hsu, H. M. Lee, A. T. Linde and S. Sacks (2018), Seismicity controlled by a frictional afterslip during a small magnitude seismic sequence ($M_L < 5$) on the Chihshang Fault, Taiwan, *J. Geophys. Res. Solid Earth*, *123*(2), 2003–2018, doi:10.1002/2017JB015128.

Eshelby, J. D. (1957), The determination of the elastic field of an ellipsoid inclusion and related problems, *Proc. R. Soc. London A*, *241*, 376–396.

Huang, K. C., H. Kao and Y. M. Wu (2000), The determination of M_L-M_w in Taiwan, in *Proceedings of the 8th Annual Meeting of Geophysical Society of China*, Taipei City, Taiwan, pp. 193–201.

Kanamori, H. and D. L. Anderson (1975), Theoretical basis of some empirical relation in seismology, *Bull. Seismol. Soc. Am.*, 65(5), 1073–1095.

Lin, J. T., W. L. Chang, D. Melgar, A. M. Thomas and C. Y. Chiu (2019), Quick determination of earthquake source parameters from GPS measurements: a study of suitability for Taiwan, *Geophys. J. Int.*, *219*, 1148-1162.

Okada, Y. (1992), Internal deformation due to shear and tensile faults in a half-space, *Bull. Seism. Soc. Am.*, *82*(2), 1018–1040.

Thomas, M. Y., J. P. Avouac, J. Champenois, J. C. Lee and L. C. Kuo (2014), Spatiotemporal evolution of seismic and aseismic slip on the Longitudinal Valley Fault, Taiwan, *J. Geophys. Res.*, *119*(6), 5114–5139.

Thomas, M. Y., J. P. Avouac and N. Lapusta (2017), Rate-and-state friction properties of the Longitudinal Valley Fault from kinematic and dynamic modeling of seismic and aseismic slip, *J. Geophys. Res.*, *122*, doi:10.1002/2016JB013615.

Wu, Y. M., R. M. Allen and C. F. Wu (2005), Revised M_L determination for crustal earthquakes in Taiwan, *Bull. Seism. Soc. Am.*, *95*(6), 2517–2524.

Table S1. Range of fault parameters considered for the grid search approach for SSE source characterization (about 6.10^8 models). Note that not all (L, R) combinations are considered for a given depth to ensure that the SSE source do not extend above the free surface. Besides, for a given depth, R is not varying with a constant step to allow a large exploration of the fault dimensions.

Depth	L (km)	R (L/W)	Slip U (m)	Magnitude	Models
1 km	0.75-6.50 (0.25)	1.2-8.4	0.025-0.3 (0.015)	3.30-5.15	$1.09.10^7$
2 km	1.0-10 (0.50)	1.2-10	0.025-0.55 (0.025)	3.30-5.80	$1.67.10^7$
3 km	1.0-13 (0.50)	1.2-9.2	0.030-0.60 (0.03)	3.30-6.05	$2.11.10^7$
4 km	1.0-15 (0.60)	1.2-10	0.030-0.60 (0.03)	3.30-6.15	$1.67.10^7$
5 km	1.0-16 (0.60)	1.2-8.5	0.030-0.69 (0.03)	3.45-6.25	$1.71.10^7$
6 km	1.5-18 (0.60)	1.2-8.0	0.030-0.75 (0.03)	3.55-6.45	$2.36.10^7$
7 km	1.5-18 (0.60)	1.2-8.0	0.030-0.75 (0.03)	3.80-6.45	$1.93.10^7$
8 km	1.5-20 (0.60)	1.2-7.0	0.030-0.78 (0.03)	3.75-6.50	$2.18.10^7$
9 km	1.5-20 (0.60)	1.2-6.5	0.020-0.80 (0.03)	3.65-6.55	$2.44.10^7$
10 km	1.5-20 (0.70)	1.2-6.0	0.020-0.83 (0.03)	3.50-6.55	$2.30.10^7$
11 km	2.0-20 (0.70)	1.2-6.5	0.020-0.86 (0.03)	3.85-6.55	$2.54.10^7$
12 km	2.0-22 (0.70)	1.2-6.0	0.020-0.89 (0.03)	3.75-6.60	$3.12.10^7$
13 km	2.0-24 (0.75)	1.2-5.0	0.01-1.0 (0.03)	3.50-6.70	$3.28.10^7$
14 km	2.0-24 (0.75)	1.2-5.0	0.02-1.10 (0.04)	3.80-6.73	$2.92.10^7$
15 km	3.0-25 (0.75)	1.2-5.0	0.02-1.10 (0.04)	3.95-6.75	$3.32.10^7$
16 km	3.0-25 (0.75)	1.2-5.0	0.01-1.56 (0.05)	3.75-6.85	$3.62.10^7$
17 km	4.0-26 (0.75)	1.2-5.0	0.1-2.0 (0.1)	4.60-6.95	$2.50.10^7$
18 km	4.0-26 (0.75)	1.2-5.0	0.1-2.0 (0.1)	4.60-6.95	$2.56.10^7$
19 km	5.0-27 (1.0)	1.2-4.7	0.1-2.0 (0.1)	4.75-7.00	$2.19.10^7$
20 km	5.0-28 (1.0)	1.2-4.5	0.2-2.4 (0.1)	4.95-7.00	$2.70.10^7$
21 km	5.0-28 (1.0)	1.2-4.5	0.2-2.6 (0.2)	5.00-7.05	$1.49.10^7$
22 km	5.0-28 (1.0)	1.2-4	0.2-2.6 (0.2)	5.00-7.05	$1.68.10^7$
23 km	6.0-28 (1.0)	1.2-4	0.2-2.8 (0.2)	5.00-7.10	$1.50.10^7$
24 km	6.0-28 (1.0)	1.2-5	0.2-2.8 (0.2)	5.00-7.10	$1.14.10^7$
25 km	6.0-28 (1.0)	1.2-4	0.2-2.8 (0.2)	5.00-7.10	$1.39.10^7$
26 km	7.0-28 (1.0)	1.2-4	0.2-2.8 (0.2)	5.15-7.10	$1.66.10^7$
27 km	8.0-30 (1.0)	1.2-4	0.2-3.0 (0.2)	5.20-7.15	$1.86.10^7$

Table S2. Details about the retained microearthquakes from the Taiwan Event Catalog (TEC) for the search period (2003-2019). Events have magnitudes ranging from 1.43 to 2.90, including 10 events with $M_L < 2$. Events 1 to 3 occurred during the slow slip episode. Earthquakes depicted in bold are events remaining after relocation of the multiplet.

Ref.	Day	Time	Latitude (°)	Longitude (°)	Depth (km)	M_L
1	02/05/2011	16:11:09,29	23.1588	121.3230	16.3	1.94
2	02/05/2011	16:13:29,43	23.1578	121.3075	15.1	1.75
3	02/05/2011	16:48:32,96	23.1670	121.3128	13.5	1.99
26	05/13/2005	05:21:04.23	23.1640	121.2931	11.7	1.60
40	12/31/2005	23:40:02.14	23.1561	121.3318	17.5	2.90
44	11/23/2006	09:47:21.97	23.1601	121.2991	14.0	1.60
54	04/02/2008	09:32:45.63	23.1465	121.3856	20.5	2.76
55	04/02/2008	09:43:35.55	23.1456	121.3236	17.8	1.66
57	04/04/2008	10:14:03.29	23.1586	121.3140	14.9	1.43
66	04/14/2009	02:19:00.92	23.1485	121.3140	17.1	1.70
76	11/24/2012	01:00:46.37	23.1550	121.3163	16.1	2.31
77	11/24/2012	01:01:05.32	23.1681	121.3551	17.3	2.09
106	02/07/2018	22:09:45.32	23.1515	121.3560	19.6	1.69
112	09/12/2018	15:39:57.29	23.1670	121.3530	15.8	1.62

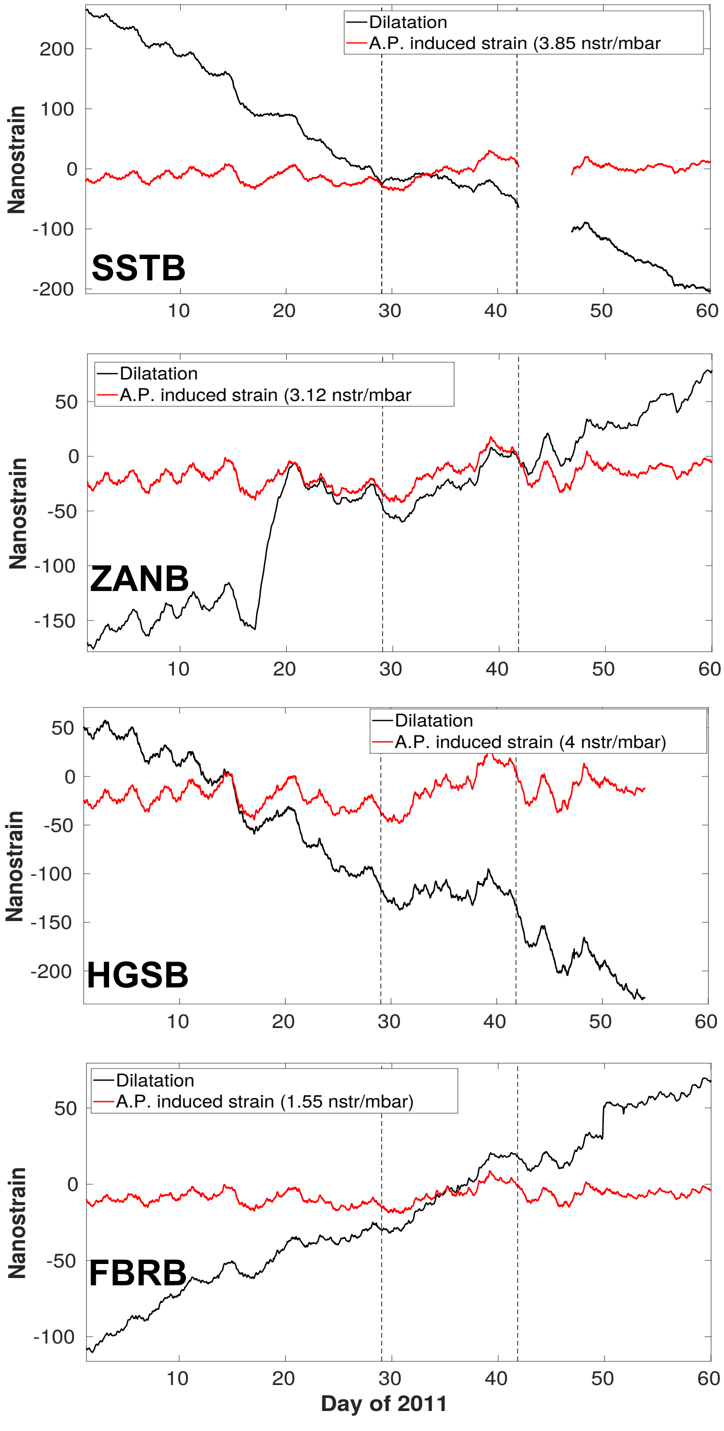

Figure S1. Detided (the solid-Earth and ocean tides) strain signals over a 2-month period (January-February 2011). Expansion is positive. Signals are not detrended and not corrected for air pressure (A. P.) induced strain. Vertical black dashed lines span the occurrence of the SSE episode (days 29 to 41.8). SSTB experiences a power outage during days 42 to 47.

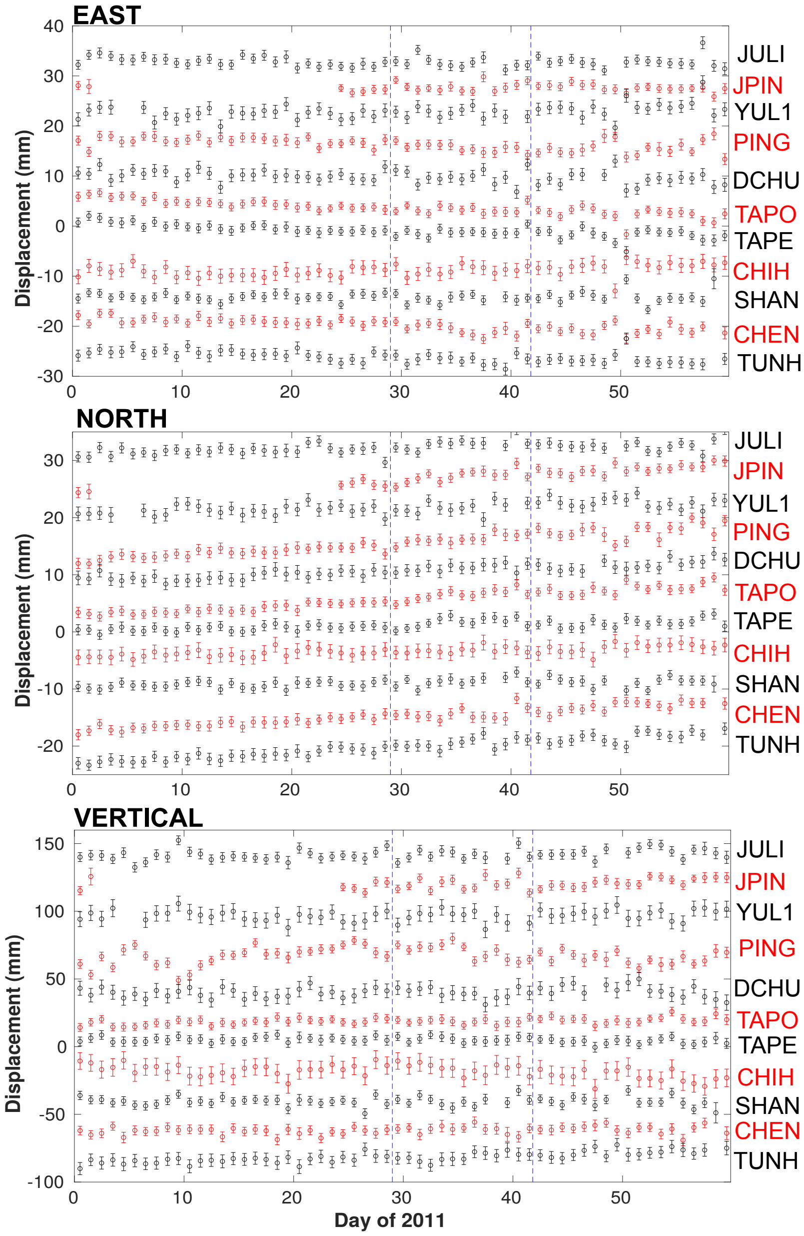

Figure S2. Daily GPS positions over a 2-month period (January-February 2011) corrected for common mode errors. Time-series are modeled using a linear trend, semi-annual and annual variations, offsets due to earthquakes or instrumental changes and postseismic transients. The spatially correlated common mode noises are estimated as the average of staking all residual time series at adjacent stations and then removed from observations. Uncertainties are about ± 1 mm for the horizontal components and about ± 5-8 mm for the vertical component. Blue lines span the occurrence of the SSE episode. The slow slip episode has not been detected by GPS stations.

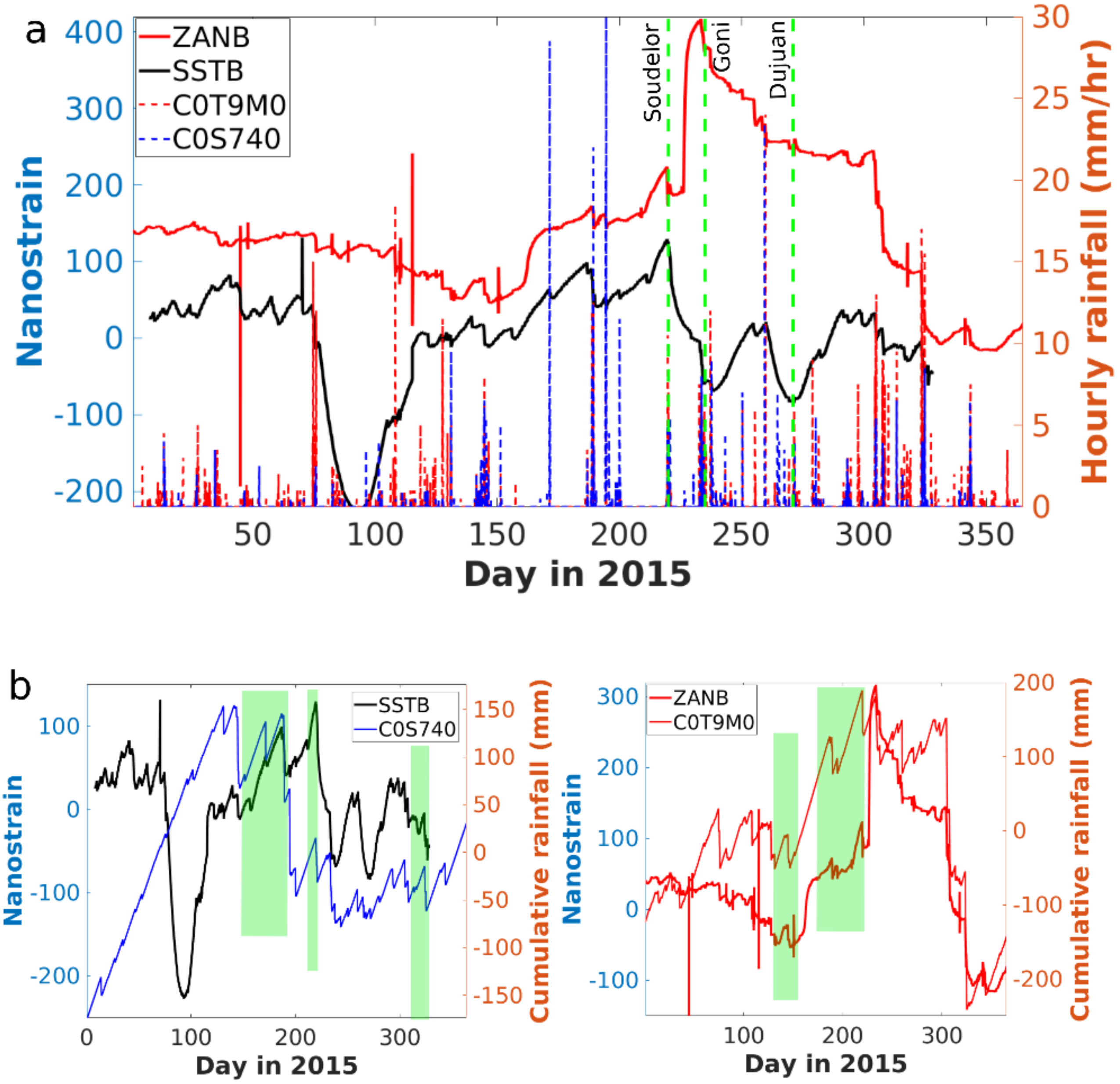

Figure S3. (a) Residual dilatation signals at SSTB and ZANB stations and hourly rainfall signals (C0T9M0 and C0S740) over a 1-year period. Expansion is positive. Vertical green dashed lines denote the main typhoons in 2015. (b) Comparison between dilatation and detrended cumulative rainfall computed for the station close to each strainmeter. Periods during which volumetric strain is likely modulated by the cumulative rainfall loading are denoted by green boxes.

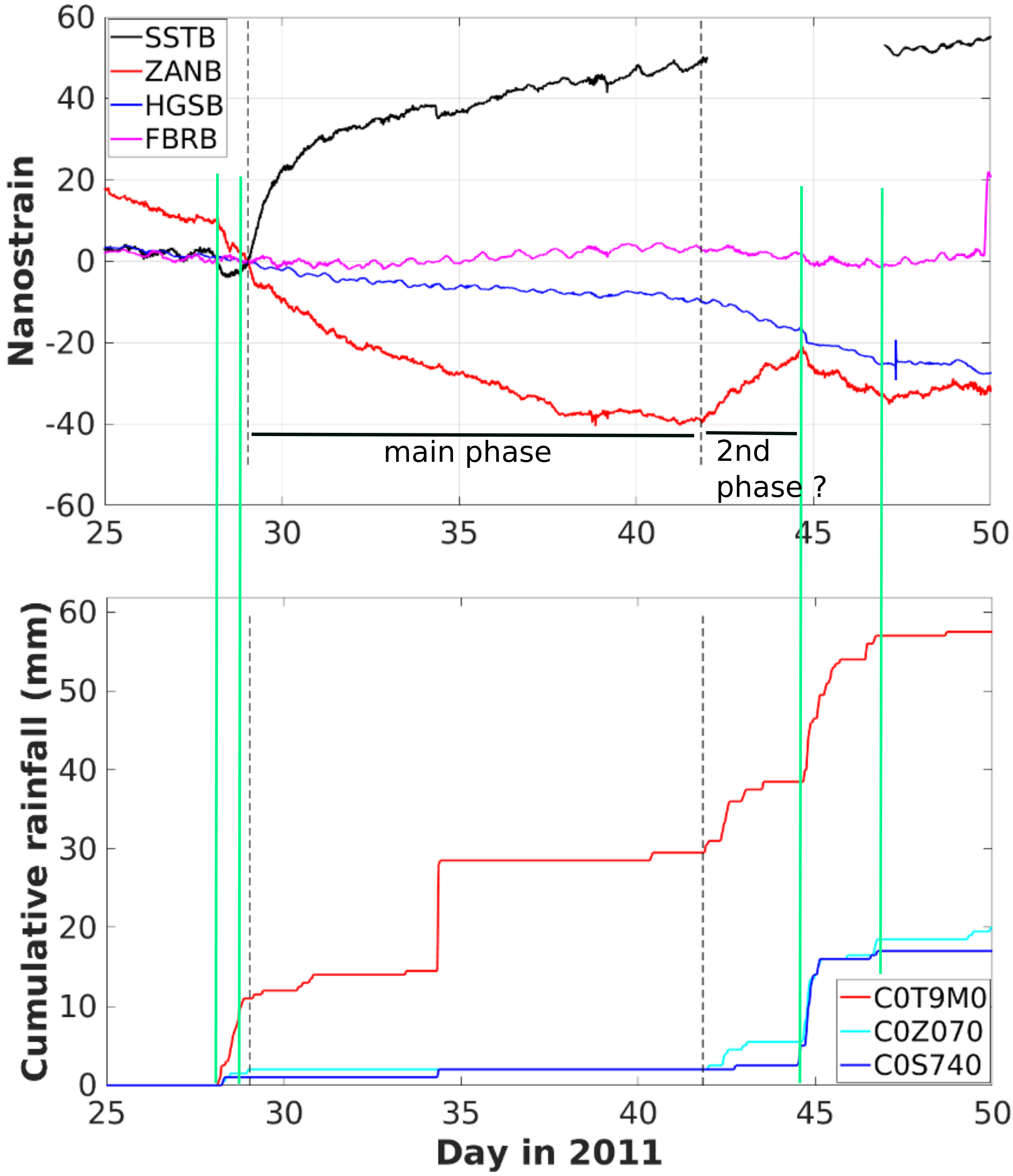

Figure S4. (a) Residual strain signals (expansion is positive) and (b) cumulative rainfall signals from days 25 to 50 in 2011. Vertical black dashed lines span the occurrence of the SSE episode (days 29 to 41.8). Vertical green lines indicate rainfall episodes before (day 28.2) and after (days 44.6-47) the SSE episode. The SSE occurs during a period of minimum precipitation. Note that SSTB experiences a power outage during days 42 to 47.

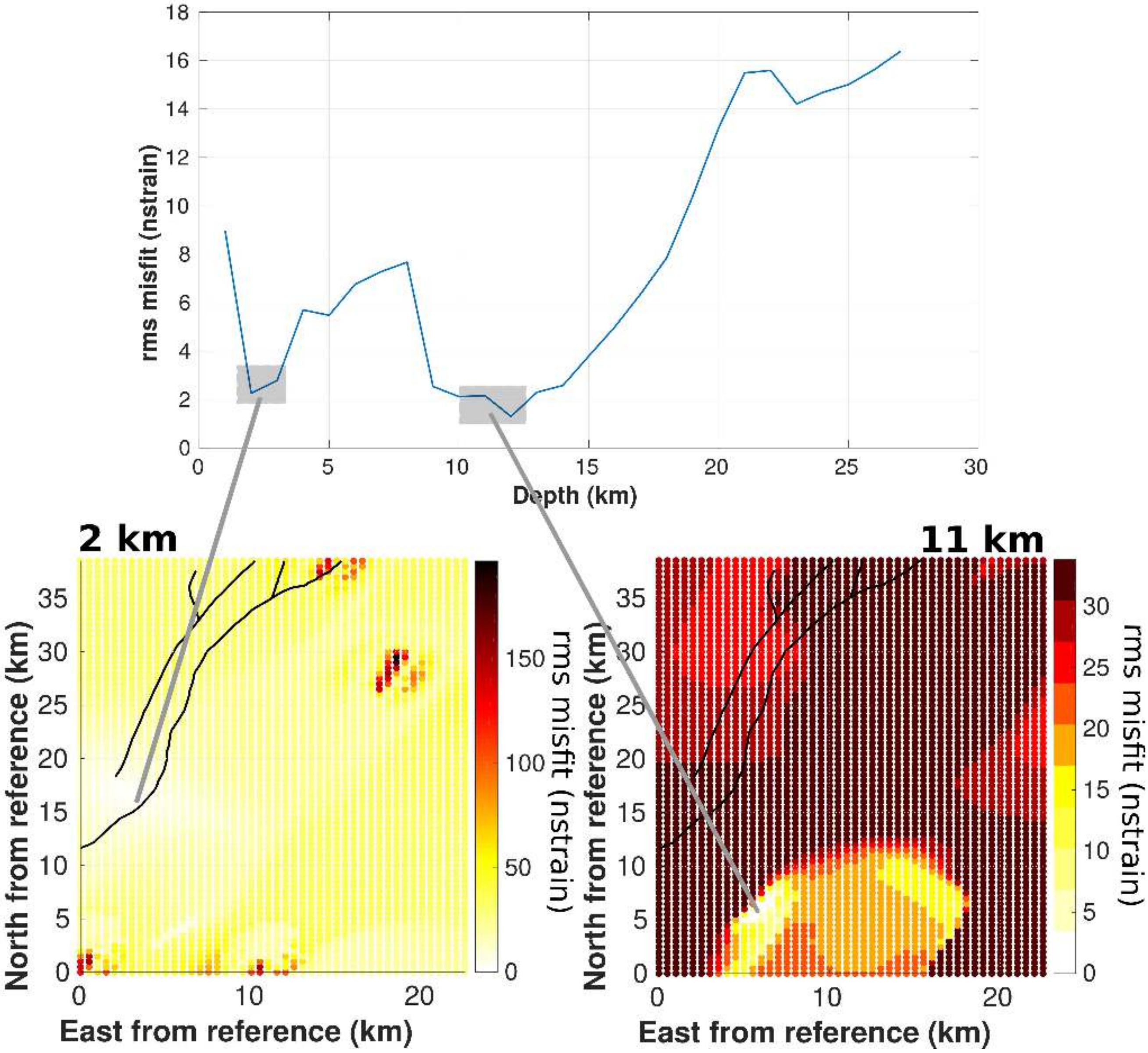

Figure S5. Misfit function dependence with source depths. Two source regions associated with low rms misfit (< 2.2 nϵ) are found: a shallow source ($\sim$ 2-3 km) and a source located at intermediate depth (10-12 km). Gray lines depict the source east-north locations for depths of 2 km and 11 km, respectively. FBRB station is the reference for the grid search.

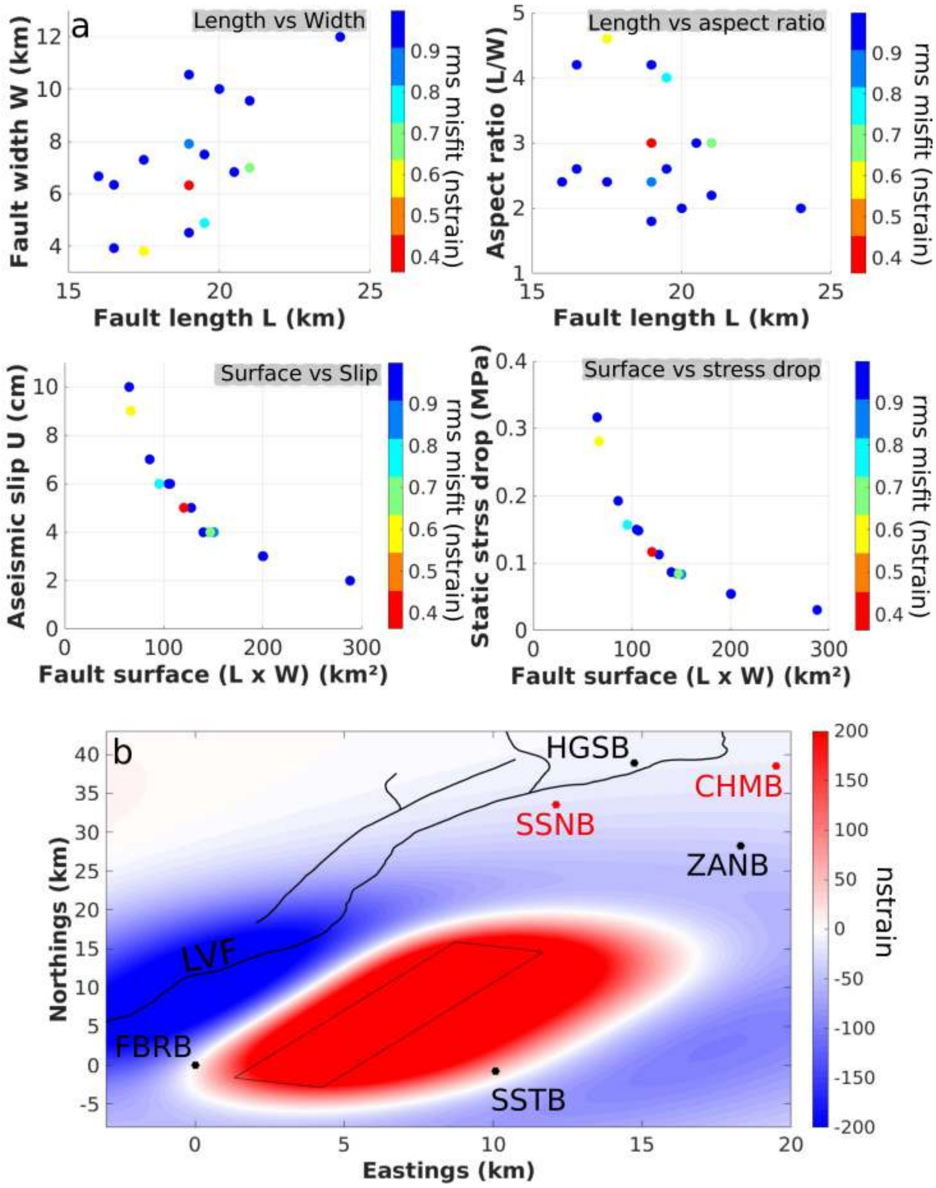

Figure S6. (a) Fault characteristics for sources with minimum misfit (rms < 1 nϵ) located at intermediate depth on the LVF (10.5 to 11.5 km). Red dot denotes the characteristics associated with our best source model (rms $= 0.36$ nϵ). (b) Volumetric strain field (expansion is positive) in the case of our best source model. Insignificant change for FBRB can be explained by a nodal plane (i.e., a plane that divides compressive from extensive areas) passing through the station location. The black rectangle denotes the surface projection of the SSE fault plane. Black and red labels denote operating and non-operating stations during the 2011 SSE, respectively. LVF: Longitudinal Valley fault.

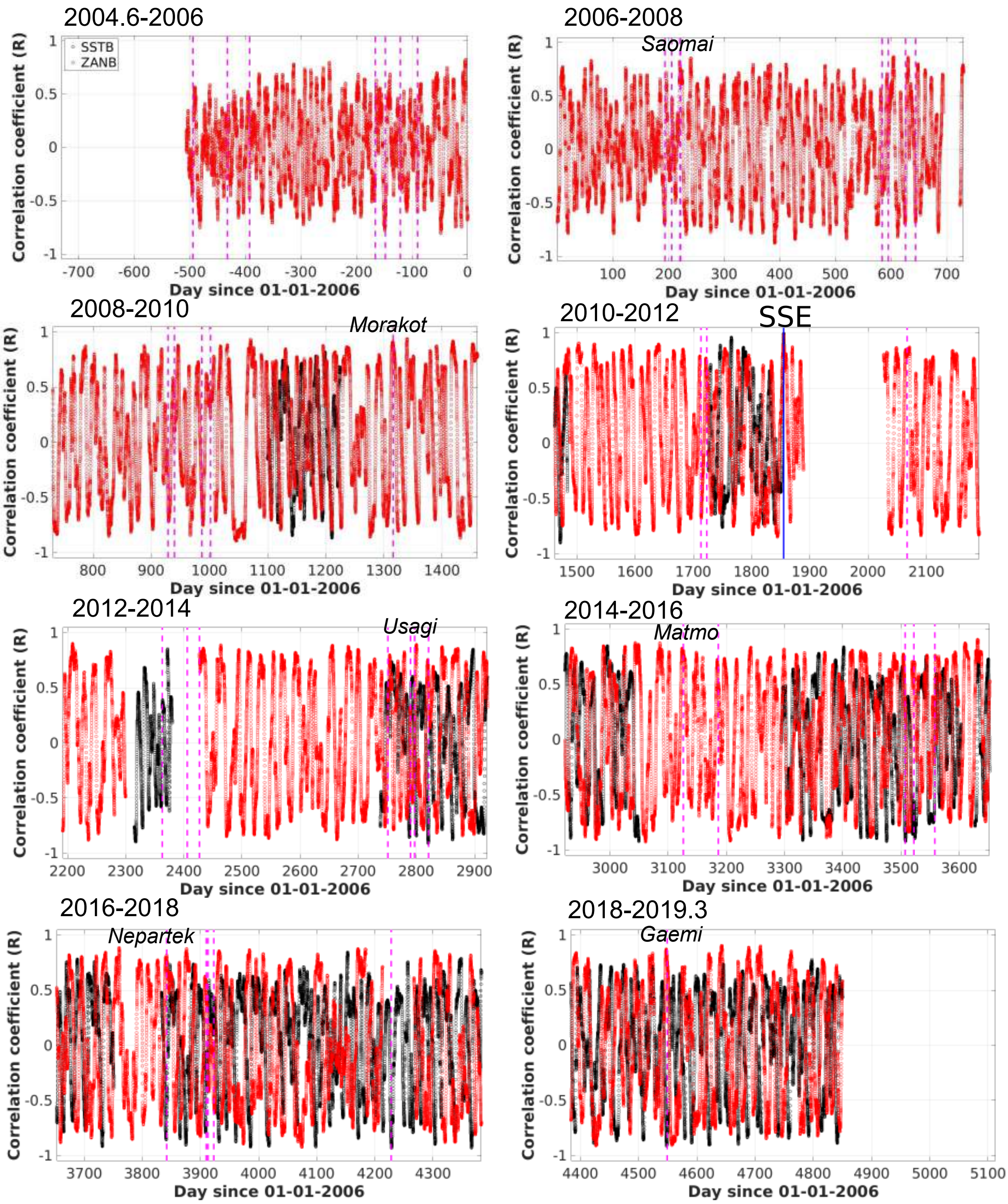

Figure S7. Template matching results for stations SSTB (black circles) and ZANB (red circles) for the period 08/2004-04/2019. The correlation coefficient (R) is expressed as values between +1 and -1 (perfect positive to perfect negative correlation). The magenta dashed lines indicate the timing of major tropical typhoons which made landfall in Taiwan. The blue line denotes the 2011 SSE occurrence.

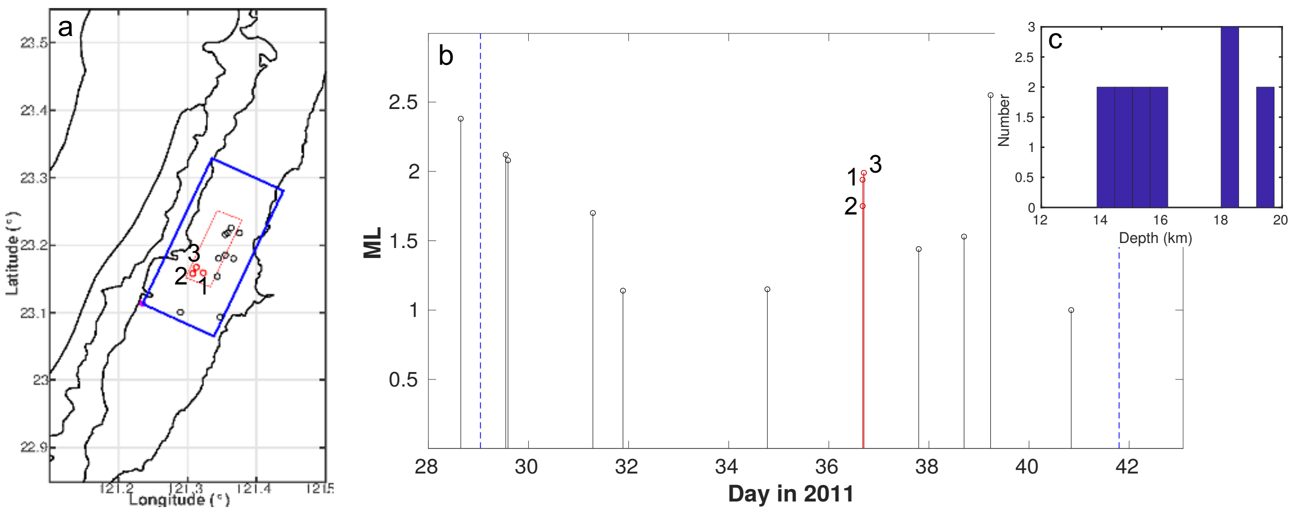

Figure S8. (a) Surface projection of the SSE source plane (red rectangle) and the selected area for seismicity analysis (between 5-20 km depth, blue rectangle). Black and red dots denote regular and repeating earthquakes (events 1-3) occurring in the selected area during the SSE episode, respectively. (b) Magnitude-time distribution of earthquakes ($M_L \geq 1$) in the selected area during the SSE episode (from days 29 to 41.8, vertical dashed blue lines). (c) Depth distribution of the events. No abnormal changes in seismicity or non-volcanic tremors are detected during the SSE episode. The seismicity rate is about 0.92 event/day ($\sim$ 335 events/year) which is on the higher bound of the annual seismicity rate in the selected area estimated from 2006 to 2015 (280 $\pm$ 50 events/year with $M_L \geq 1.0$).

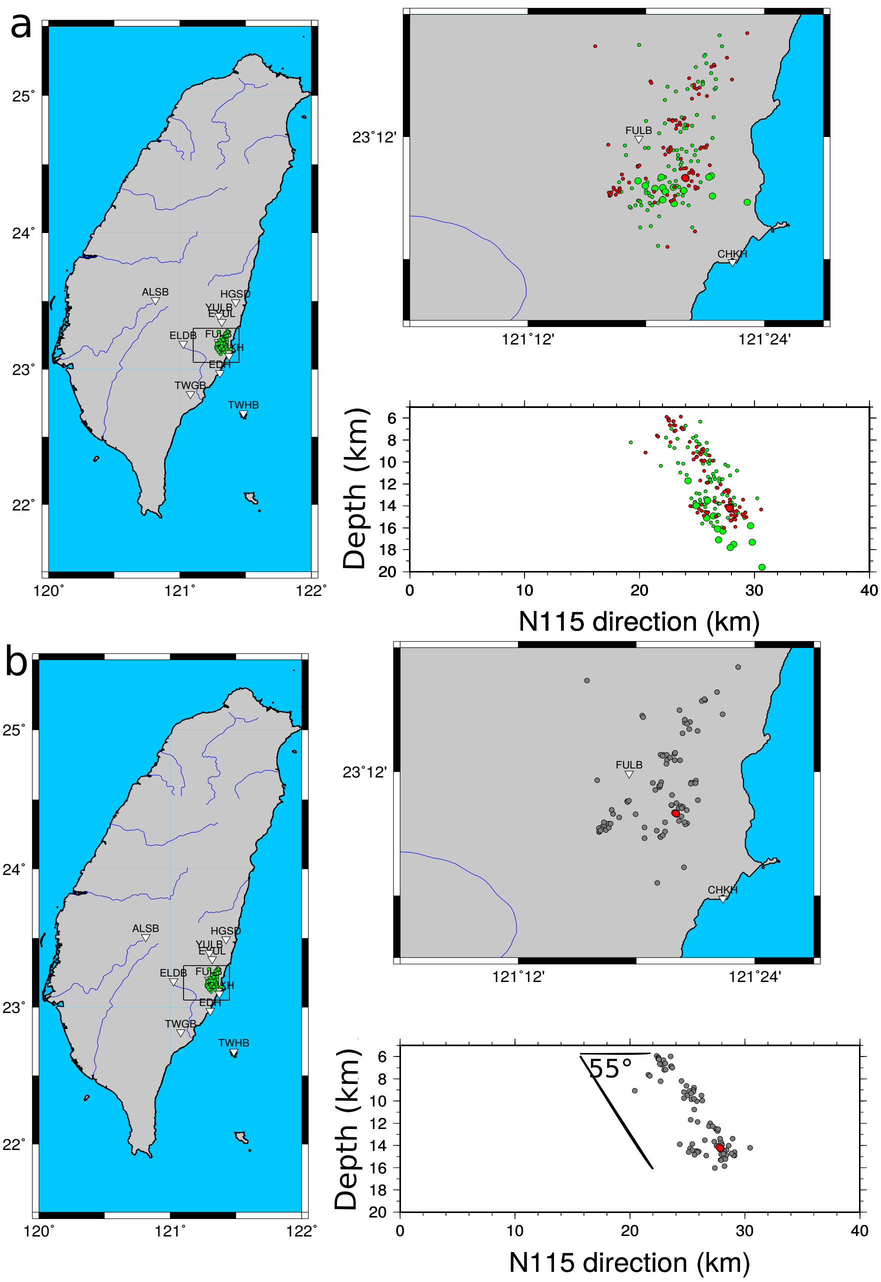

Figure S9. (a) Joint relocation of the multiplet and 100 regular events (i.e., non clustered) (with $M_L \geq 2.50$) selected near the SSE source region on the LVF. Green and red dots denote the catalog locations and double-difference relocations, respectively. Small and large dots represent the regular events and the events inside the multiplet, respectively. Inverted triangles denote broadband seismological stations used for the relocations. Black rectangle depicts the zoomed region where seismicity is relocated. (b) Same as for (a) for relocated seismicity (gray dots: regular events, red dots: relocated multiplet).

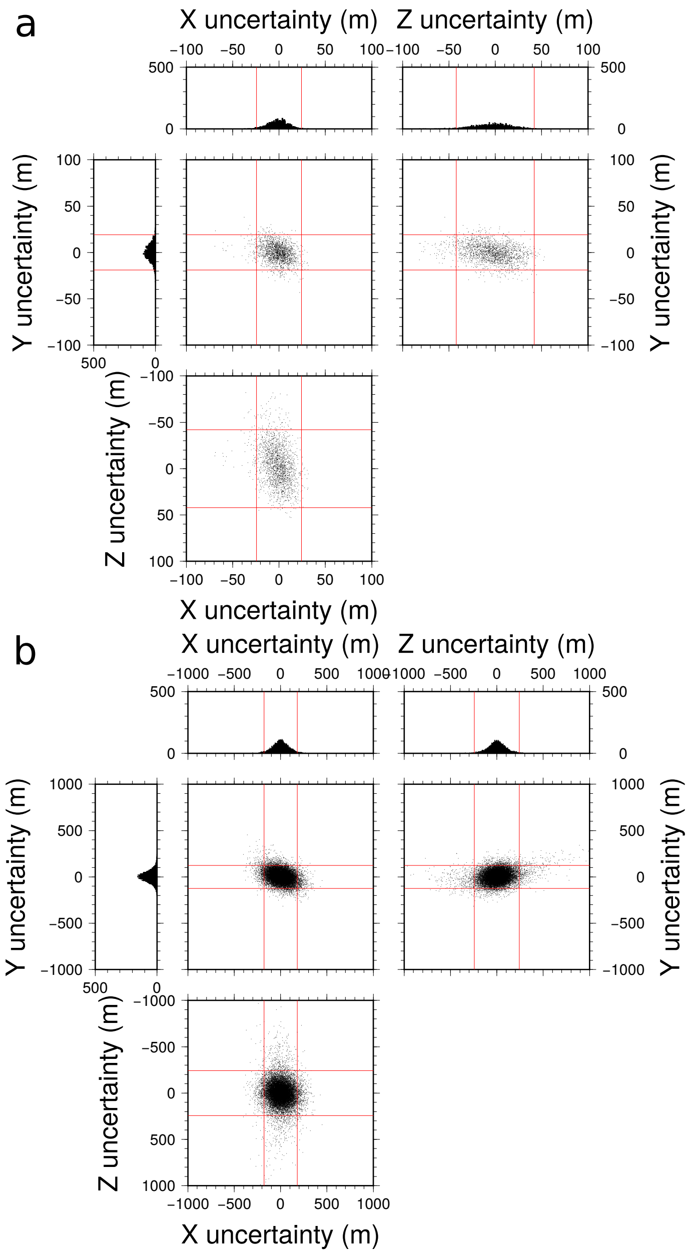

Figure S10. Bootstrap analysis of the residuals of relocations using double-difference: (a) relative location uncertainty inside the multiplet and (b) absolute location uncertainty of the multiplet. P/S-wave time delays obtained from manual picks and cross-correlations are replaced by samples drawn in the residual time distributions given by the double-difference. Samples are relocated to determine the shift location related to the residual times. The process is repeated 200 times and an estimate of the relative uncertainties is given by the distribution of the cumulative repetitions. Red lines contain 95% of the points (2σ).

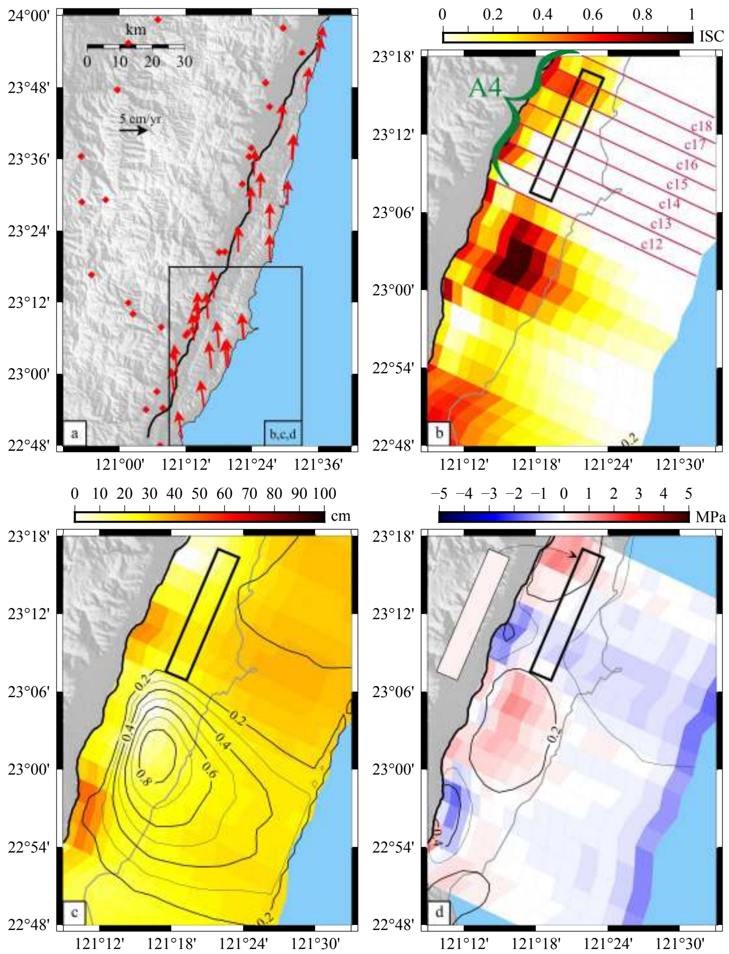

Figure S11. (a) Secular motion of the Coastal Range relative to the Central Range as computed in *Thomas et al.* [2014]. The projection of this surface field onto the fault gives the long-term slip rate of the LVF. (b) Interseismic coupling (ISC) distribution along the LVF quantifying the degrees of locking of the fault (ISC = 1, the fault patch is fully locked, ISC = 0, the patch is creeping at the long-term slip rate). The coupling map is computed in *Thomas et al.* [2014] using data (InSAR, cGPS, creepmeter, levelling) acquired between the 01/01/1994 and the 26/11/2010. (c) 7-year cumulative slip (01/1997-12/2003) prior to the December 2003 earthquake. (d) Related δCFF resolved onto the LVF fault plane. The plane depicted on the side represents δCFF computed for a fixed rake of 70°. Black star denotes the Chengkung earthquake epicenter and black rectangle outlines the SSE rupture area. Black curves give the contour lines of the coseismic (b,c) and the preseismic (d) slip distribution models (in meter).

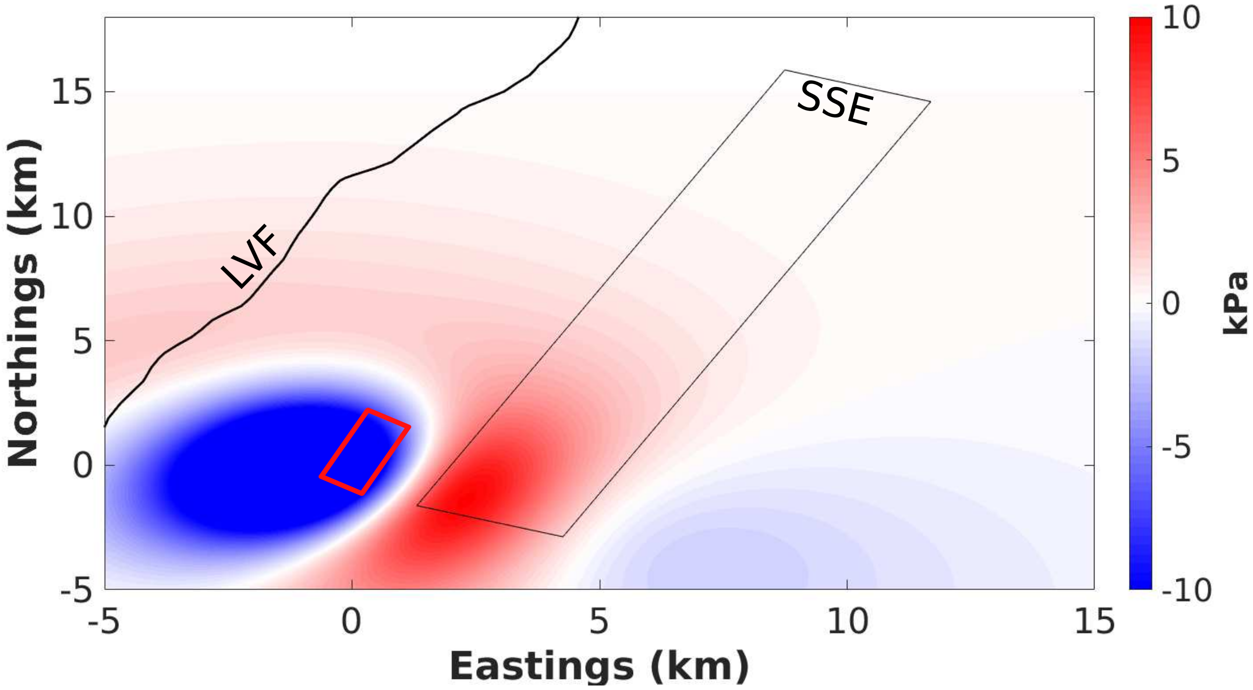

Figure S12. Static Coulomb stress changes caused by the 2010 afterslip source (L x $W \sim 2$ km x 1.5 km, $D \sim 0.12$ m) in the SSE source region at a mean depth of about 11 km. Receiver fault characteristics are: strike = 23°/dip = 60°/rake = 70°. The 1-month long afterslip with geodetic moment of about 4.8 occurred in April 2010 [*Canitano et al.*, 2018] (about 9 months prior to the SSE), about 2 km updip from the SSE source. Slip is favored in the SSE source region (maximum $\delta CFF \sim +10$ kPa). The black and red rectangles denote the surface projection of the SSE fault plane and of the afterslip plane, respectively. LVF: Longitudinal Valley fault.

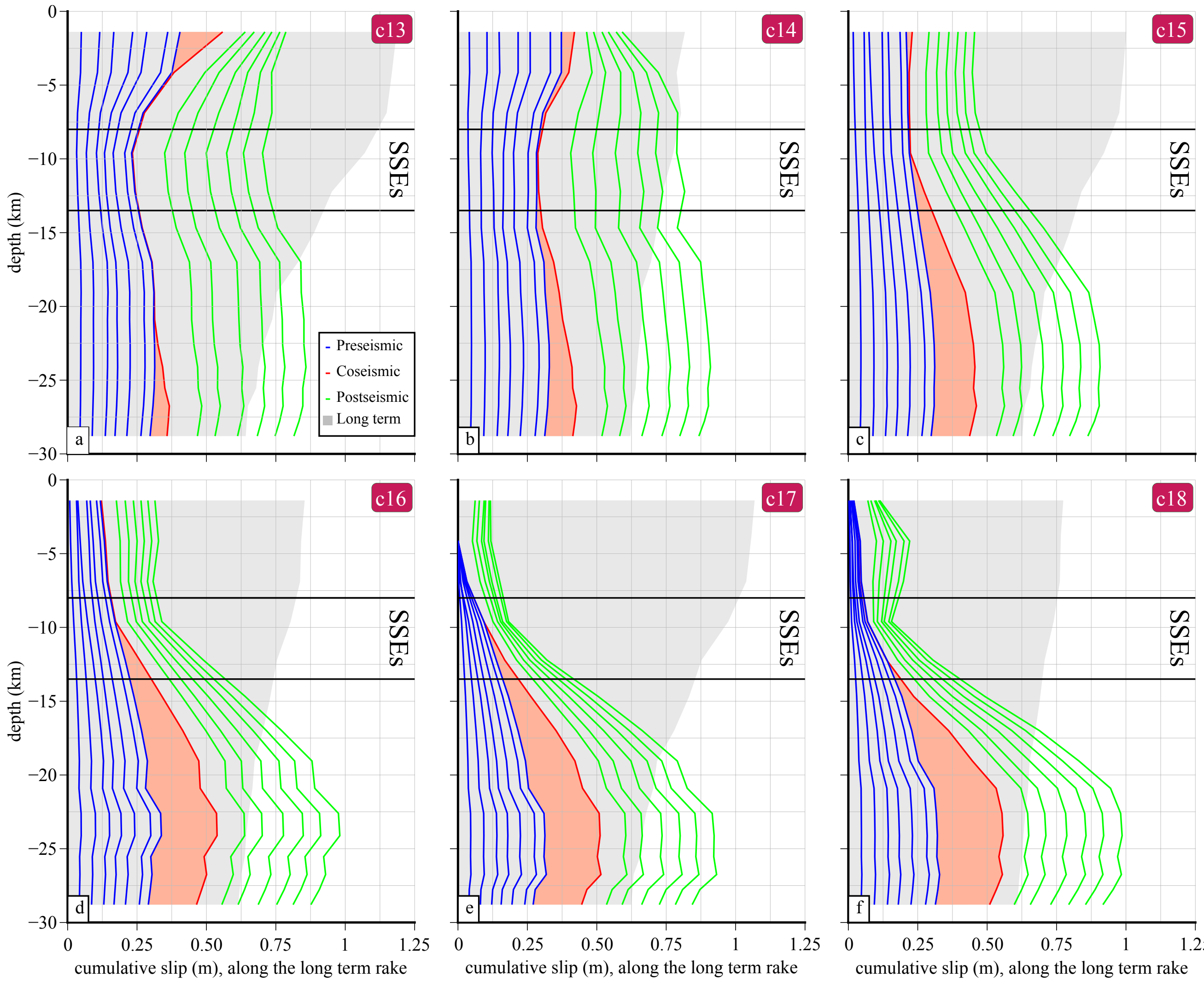

Figure S13. Cumulative slip along the long-term rake for the columns c13 to c18 within the A4 area (see Figure S11b for the location). Isochrons are plotted with an increment of 1 year for the 7-yr preseismic (blue) and the 7-yr postseismic (green) periods; red and grey shading give respectively the coseismic slip and the total motion of the fault if it had crept at the long term slip rate during those 14 years.

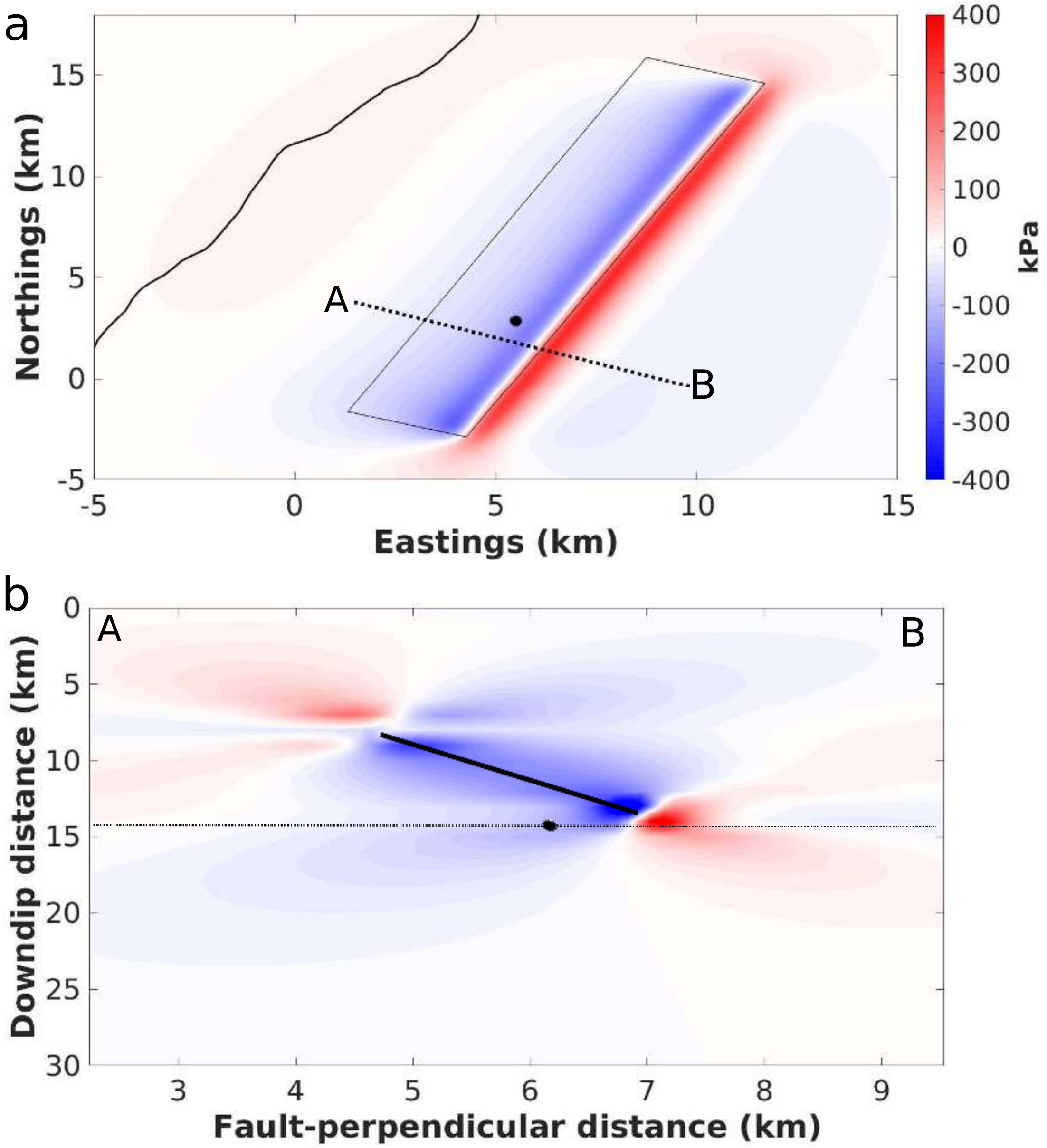

Figure S14. Static Coulomb stress changes caused by the 2011 SSE on a receiver fault with characteristics: strike = 23°/dip = 60°/rake = 70°. (a) Stress changes along a horizontal plane at a mean depth of 14.2 km (REs mean depth). The black rectangle denotes the surface projection of the SSE fault plane. Dashed black line indicates the cross-section A-B in (b). (b) Cross-section perpendicular to the LVF. The black line denotes the SSE fault plane. The black dots denote the events identified during the SSE episode. The horizontal dashed line indicates the mean depth of the cluster. REs occurred when 85% of total aseismic slip was relieved (4.25 cm).

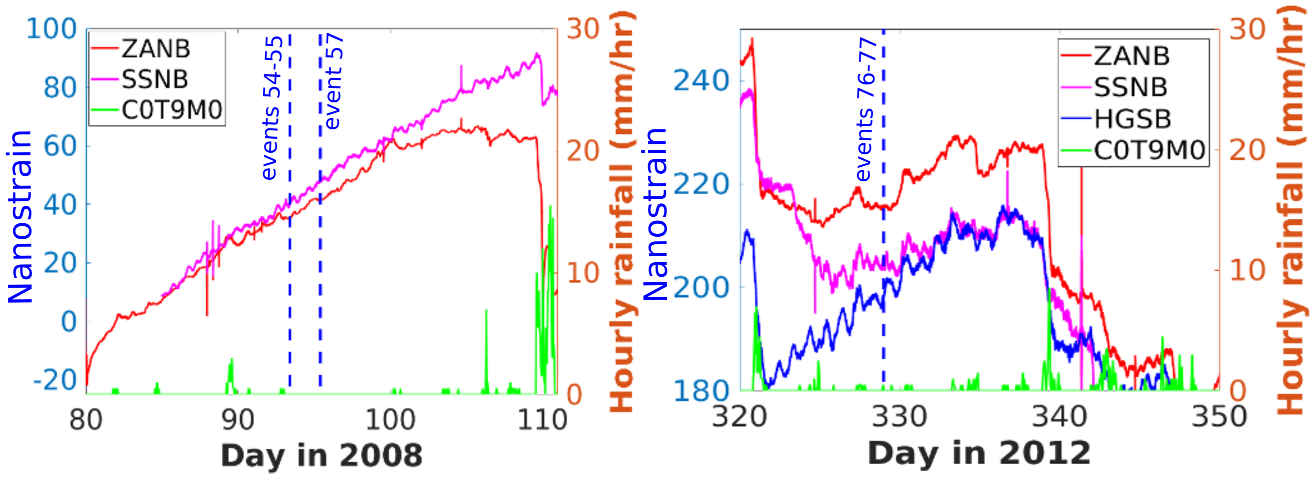

Figure S15. Evolution of strain signals over a 1-month period during burst-type repeaters (vertical blue dashed lines): (left) events 54-55 and 57 in April 2008 and (right) events 76-77 in November 2012. The green curve denotes hourly rainfall data recorded by station C0T9M0 (Figure 1).